

A Diagnostic Modeling Study of the Trailing Stratiform Region of a Midlatitude Squall Line

STEVEN A. RUTLEDGE

Department of Atmospheric Sciences, Oregon State University, Corvallis, OR 97331

ROBERT A. HOUZE, JR.

Department of Atmospheric Sciences, University of Washington, Seattle, WA 98195

(Manuscript received 30 July 1986, in final form 13 April 1987)

ABSTRACT

A kinematic model with continuity equations for sensible heat, water vapor, cloud water, cloud ice, rain, snow, and graupel is used to determine the steady state thermodynamic and microphysical processes associated with the observed mesoscale air motion fields in the trailing stratiform region of the 22 May 1976 Oklahoma squall line. Two versions of the observed air motions are used: a low-resolution but areally extensive flow pattern derived from the composite sounding data of Ogura and Liou, and a high-resolution but less areally extensive flow field obtained from the dual-Doppler radar analysis of Smull and Houze.

Model calculations based on the high-resolution Doppler-derived mesoscale air motions show that the location and horizontal scale of the region of most intense stratiform precipitation are determined by the pattern of horizontal transport and fallout of snow and low-density graupel particles advected into the stratiform region from the leading line of convective cells. The stratiform-region water budget implied by these calculations further indicates that the amount of stratiform rain reaching the surface is considerably enhanced by the passage of these particles through the region of mesoscale upward motion in the stratiform cloud behind the convective line. Vapor deposition onto existing ice particles and the collection of snow generated by the mesoscale ascent are the dominant growth processes in the stratiform region. Simulations using the low-resolution sounding-derived air motions as input to the model show that the mesoscale updraft accounts for the extensive nonraining stratiform cloud to the rear of the surface precipitation area.

1. Introduction

Squall lines characterized by trailing mesoscale regions of stratiform precipitation occur in both the tropics and midlatitudes. These interesting and exciting storms have attracted the attention of researchers for over four decades. The tropical lines have been described and analyzed by Hamilton and Archbold (1945), Zipser (1969, 1977), Houze (1977), Gamache and Houze (1982, 1983, 1985), Chong (1983), Houze and Rappaport (1984), Barnes and Sieckman (1984), Sommeria and Testud (1984), Rutledge (1986), Wei and Houze (1986), and Hauser and Amayenc (1986). Midlatitude cases have been examined by Newton (1950), Fujita (1955), Pedgley (1962), Ogura and Liou (1980), Smull and Houze (1985, 1986) and Srivastava et al. (1986).

A question that has arisen from these studies is: *What are the origins and growth mechanisms of particles that fall in the form of stratiform precipitation to the rear of the moving convective line?* Examination of the budget of condensed water indicates that the condensate in the stratiform region is partly provided by advection of hydrometeors from the leading convective region into the stratiform zone and partly by condensation

(or deposition) of vapor resulting from ascent within the stratiform cloud deck itself (Gamache and Houze, 1983; Chong, 1983). Houze (1981) and Smull and Houze (1985) have examined the rearward advection of hydrometeors. They note that ice particles falling from the upper portions of convective cells in the leading line can be spread a mesoscale distance rearward by strong relative horizontal flow through the system. As shown in Fig. 1, Smull and Houze (1985) hypothesized that the width and horizontal position of the most intense portion of the trailing stratiform precipitation, and its associated melting layer, could be explained by the pattern of fallout of these rearwardly advected particles. Atlas et al. (1963) made a similar suggestion to explain the breadth of stratiform radar echo in a hurricane rainband, and Lord et al. (1985) have shown by numerical modeling that the horizontal extent of melting layers in the inner-core region of hurricanes is determined by horizontal advection of the falling hydrometeors.

In an attempt to test the hypothesis of Smull and Houze (1985), Rutledge (1986) used the kinematic modeling method of Rutledge and Hobbs (1983, 1984). This method uses an observed air motion field as input to a diagnostic model consisting of thermodynamic and

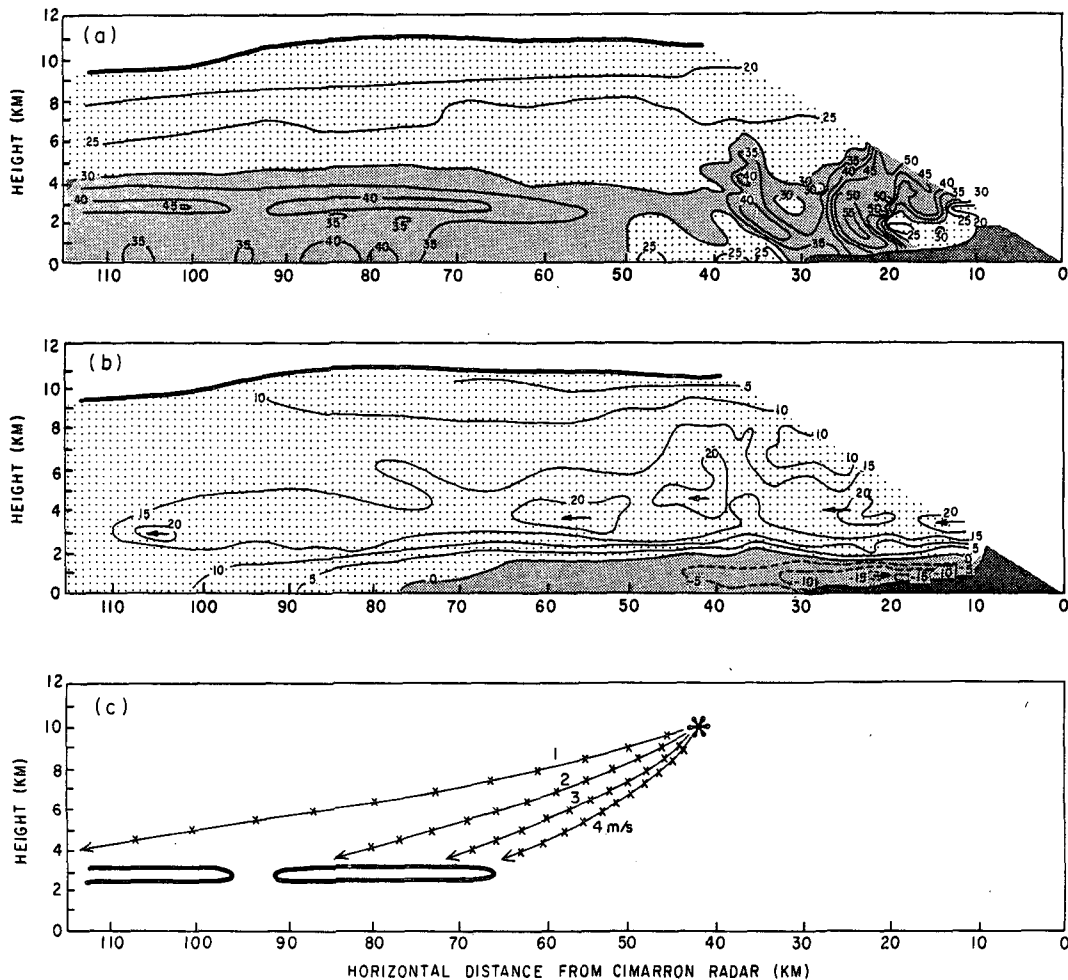


FIG. 1. Vertical cross sections of reflectivity (dBZ), horizontal wind component and ice particle trajectories for the 22 May 1976 squall line. (a) Reflectivity (dBZ), (b) horizontal wind component relative to the squall line in $m s^{-1}$, (c) deduced ice particle trajectories using the data shown in (b) along with assumed ice particle fallspeeds (labeled 1–4 $m s^{-1}$). The contour marking in (c) denotes the 40 dBZ contour marking the bright band. (Adapted from Smull and Houze, 1986.)

water budget equations. These equations are integrated to find the steady state fields of temperature, water vapor, cloud water, cloud ice, rain, snow, and graupel that are consistent with the observed airflow. Rutledge (1986) used Gamache and Houze's (1982) tropical squall-line airflow derived from composite analysis of rawinsonde data. The resulting calculations did not verify the Smull and Houze (1985) hypothesis. Instead, it was concluded that ice particles were not advected significantly rearward and the stratiform rain was the result of ascent in the trailing stratiform cloud deck. However, we now believe that this result was produced by the low resolution of the input flow field obtained from the composite analysis of soundings. In the present paper, we will show that when a high-resolution airflow derived from dual-Doppler radar data is used as input to the model, the hypothesis of Smull and Houze (1985) is verified. The dual-Doppler observa-

tions capture the details of the rearward flow exiting the convective region, and the pronounced melting layer of the stratiform region is then indeed inferred to have been produced by the fallout of ice particles carried rearward from a location at upper levels in the convective region.

2. The case chosen for study

Our study is based on model calculations carried out to represent a particular storm, the Oklahoma squall line of 22 May 1976. It was possible for us to conduct a further test of the Smull–Houze (1985) hypothesis because of the availability of both a compounding sounding analysis (Ogura and Liou, 1980) and a dual-Doppler analysis (Smull and Houze, 1986) for this case. The composite sounding analysis of Ogura and Liou (1980) had a grid resolution of 45 km. This

resolution is similar to the 50-km interpolated grid resolution of the Gamache and Houze (1982) tropical squall-line composite wind pattern used by Rutledge (1986), and it will be seen later in this paper that model results obtained using the Ogura and Liou (1980) composite wind field strongly resemble those of Rutledge (1986). They also do not confirm the SH hypothesis. However, the dual-Doppler radar-derived wind field of Smull and Houze (1986) has a resolution of just a few kilometers, and model calculations obtained using this higher-resolution wind field as input differ substantially from those using the lower-resolution Ogura and Liou (1980) wind field. These calculations do confirm the Smull and Houze (1985) hypothesis.

3. Modeling technique and input data

a. Approach

The approach of this paper is similar to that of Rutledge (1986). The mesoscale wind field (horizontal and vertical components) within the cloud system is obtained from observations. This wind field is then assumed to apply in the model domain and held constant while thermodynamic and water continuity equations are integrated to diagnose the steady state fields of temperature, water vapor, and various types of hydrometeors that are consistent with the observed winds. The model domain comprises only the stratiform region of the squall system. The influence of the convective line on the stratiform region is parameterized by specifying vertical profiles of ice and water on the vertical boundary adjacent to the convective region. The following subsections briefly describe the model and elaborate on the observed wind fields and other input quantities required to test the Smull and Houze (1985) hypothesis.

b. The model

The model used in this study is a two-dimensional version (x - z , where x is perpendicular to the squall line and z is height) of the model used by Rutledge (1986). The three-dimensional simulations discussed by Rutledge (1986) indicated that the stratiform region could be regarded as two-dimensional during the mature stage; hence the use of a 2-D model for this study is appropriate. Since this model is described in detail in Rutledge and Hobbs (1983, 1984), only some of its highlights will be given here. Continuity equations are included for temperature (T) and the mixing ratios of water vapor (q_v), cloud water (q_c), cloud ice (q_i), rain (q_r), snow (q_s) and graupel (q_g). Particle size distributions for the fields of q_r , q_s and q_g are assumed to follow inverse exponential distributions of the form

$$N(D) = N_0 e^{-\lambda D} \quad (1)$$

where N_0 is the slope intercept value (m^{-4}) and λ (m^{-1}) is the slope of the distribution. This assumption allows the use of bulk parameterizations of warm and cold

cloud microphysical processes, including condensation, evaporation, autoconversion, collection of cloud water by rain, riming, aggregation, melting, and freezing. A schematic diagram indicating all of the microphysical processes included is shown in Fig. 1 of Rutledge and Hobbs (1984).

The thermodynamic and water continuity equations are integrated in time until a steady state is reached. The horizontal and vertical wind velocity components throughout the domain are assigned observed values and held constant throughout the integration. The initial temperature and water vapor mixing ratio throughout the domain are based on sounding data taken from Ogura and Liou (1980). The initial values of the hydrometeor mixing ratios (q_c , q_i , q_r , q_s and q_g) are zero except on the boundary adjacent to the convective region.

For testing the Smull and Houze (1985) hypothesis, the most critical input data are the mesoscale winds obtained from observations and the assumed vertical distribution of hydrometeors on the vertical wall constituting the stratiform regions' boundary with the convective region. Since the system-relative horizontal flow on this boundary is directed from the convective to the stratiform zone, the observed mesoscale winds together with the assumed hydrometeor distribution on the boundary determine the horizontal flux of condensate from the convective line into the stratiform region. The model calculations test the Smull and Houze (1985) hypothesis by determining the cloud and precipitation pattern that develops within the stratiform domain in association with this continual advection of hydrometeors into the stratiform region from the region of convection. Because the observed wind field and distribution of hydrometeors on the boundary are so crucial, our choices for these two input features are discussed in some detail below.

c. Data for initial and boundary conditions

From this point on we will refer to Ogura and Liou (1980) by OL and to Smull and Houze (1986) by SH. As mentioned earlier, the model uses input data from the studies of OL and SH.

We will first discuss the input data from the OL study. Ogura and Liou analyzed their data relative to the moving squall line with the origin of the coordinate system placed at the leading edge of the convective line. The 45-km resolution data was interpolated for use in the model onto a 2-km horizontal grid by means of a bilinear interpolation. The data were transferred from pressure to height coordinates in accordance with the hydrostatic approximation and then interpolated to a vertical grid of 800 m. Our simulation is for the stratiform region only, which we define as all the area rearward from a point immediately behind the line of active convection as determined from radar observations. Since this convective area was approximately 40

km in width, our model grid begins at $x = -40$ km, the negative sign denoting distance rearward from the leading edge of the convective line.

The horizontal wind in the x direction, relative to the squall line (u_{rel}), and the vertical wind, are shown in Fig. 2. The horizontal flow in Fig. 2a indicates mainly flow from right to left, or front to rear relative to the moving squall line. Also indicated is some rear-to-front flow entering the grid on the extreme left between the 3.2 and 6.4 km levels. The fields of temperature and water vapor mixing ratio used as model inputs were also computed from data shown in OL. These were determined from the equivalent potential temperature analysis of OL, and interpolated to the model grid.

The horizontal and vertical wind field obtained from the dual-Doppler analysis of Smull and Houze (1986) is shown in Fig. 3. The labeling of the x -axis in the SH data corresponds directly to the x -axis in the OL plots (Fig. 2). We have averaged u_{rel} in the along line direction throughout the analysis domain of SH to arrive at the horizontal flow used in the model calculations. Their domain was 120 km wide in the x direction and 130 km wide in the y direction. The mean u_{rel} field used in our model calculations is shown in Fig. 3a. The major differences between this flow field and that shown in Fig. 2a for the OL case are that the front-to-rear flow is stronger, especially just to the rear of the convective region (right side of the cross section) and rear-to-front flow is absent. As pointed out by SH, the rear inflow did not extend forward into the domain of the dual-Doppler region at their analysis time.

The vertical motion field obtained from the dual-Doppler radar analysis of SH is shown in Fig. 3b. This field was obtained by merging their mean vertical motion profiles within two areas (see their Fig. 12). One area covered the region of $x > -72$ km (referred to as the "transition region" by SH) and the second $x < -72$

km (the stratiform region). The manner in which we have assembled the SH wind field does not produce a kinematic flow pattern that strictly obeys mass continuity. Violations of mass continuity are not serious for a diagnostic model of the type used here. We believe the vertical motion profiles are our best estimate of this quantity and should not be changed. Therefore, our only option is to adjust the u_{rel} field to be mass-consistent with the w field. In doing so, we found only small differences ($1-3 \text{ m s}^{-1}$) between the model u_{rel} field and the mass consistent u_{rel} field. Such small changes would not have affected the model outputs or conclusions from this study.

There are some key differences between the SH vertical motion field and the OL vertical motion field. First, the SH field indicates downward motion in the transition region ($-72 < x < -48$ km) below the 4 km ($\sim 0^\circ\text{C}$) level. The OL field indicates upward motion in this same area. Second, the updraft velocities in the transition region are greater in the SH data than in the OL data.

The thermodynamic fields and grid spacings used in the SH simulations are the same as those used in the OL cases.

d. Parameterization of the flux of condensate and water vapor from the convective line

As noted above, a key input to our calculations is the assumed vertical distribution of hydrometeors on the model domain's vertical boundary across which the relative horizontal wind brings condensate from the convective region into the stratiform region. In this study, we assume a vertical distribution of hydrometeors based on the microphysical observations of Oklahoma convective cells of Heymsfield and Hjermfelt (1984, hereafter referred to as HH).

The HH profiles were derived from data obtained

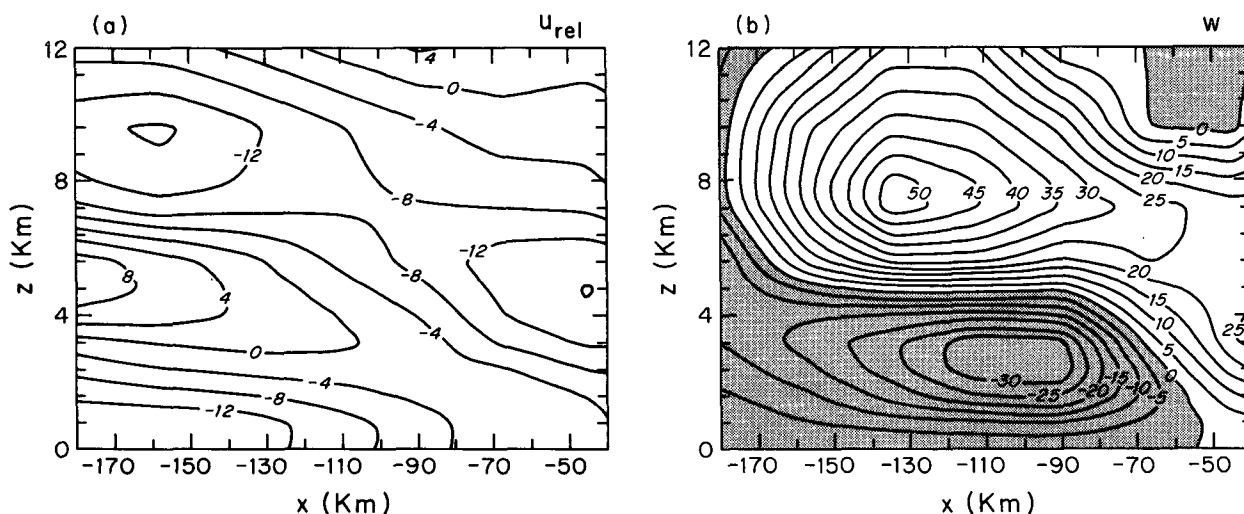


FIG. 2. Wind data from Ogura and Liou (1980) used as model input. (a) Horizontal flow in m s^{-1} relative to the squall line. (b) Vertical motion field in cm s^{-1} . Shading indicates areas of subsidence.

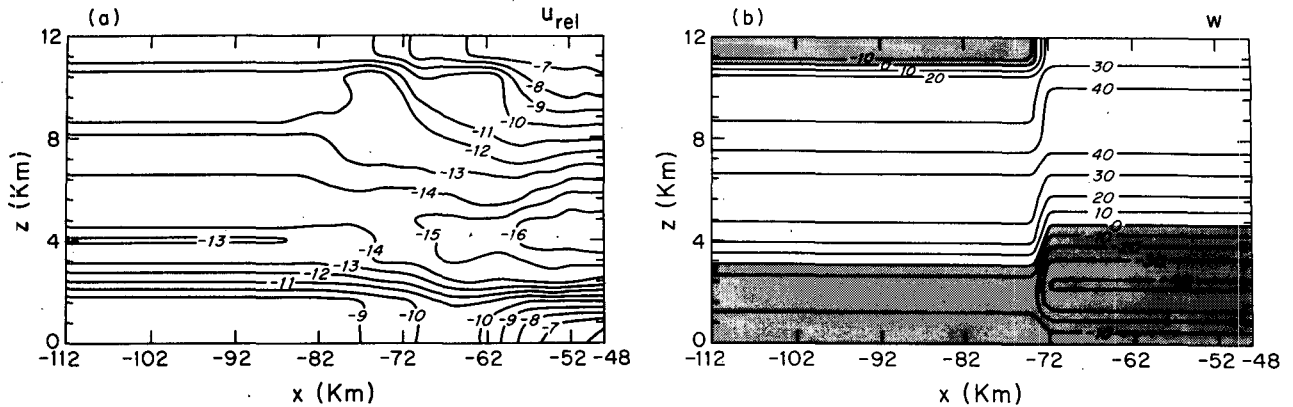


FIG. 3. Wind data from Smull and Houze (1986) used as model input. (a) Horizontal flow in m s^{-1} relative to the squall line. (b) Vertical motion field in cm s^{-1} . Shading indicates areas of subsidence.

by aircraft penetrations of Oklahoma convective cells associated with squall lines. These data were extensively tabulated and discussed by HH. They summarized the data according to ice particle concentrations and types in relation to flight-level temperature and updraft velocity. By applying assumed mean particle sizes and densities to the tabulated data, we estimated the mass concentrations for each particle type as a function of flight-level temperature (and therefore height). Assumed values included: a mean graupel diameter of $1000 \mu\text{m}$ (assumed spherical); a diameter of $1000 \mu\text{m}$ and a thickness of $40 \mu\text{m}$ for planar ice particles; a length of $500 \mu\text{m}$ and a width of $40 \mu\text{m}$ for needles; a mean diameter of $1500 \mu\text{m}$ for ice particle aggregates (assumed spherical). These dimensions were based on data described by Pruppacher and Klett (1978). The density of graupel was taken to be 0.3 g cm^{-3} and the density of all other ice particles was set at 0.1 g cm^{-3} . The data on all the crystal types other than graupel were combined to arrive at q_s .

The mass profiles for snow and graupel computed using the methodology discussed above were apparently too large as the radar reflectivity associated with the profiles was on the order of 5–10 dBZ above the observed reflectivities in the same portion of the squall line. Therefore, we decreased the amount of snow and graupel in the initial profiles until the model reflectivities came into better agreement with the observations. [A reduction of the mixing ratios by a factor of three (3) was necessary.] The resultant profiles are shown in Fig. 4. We believe our initial profiles were excessively large because the airborne data used to compute them was biased toward cell penetrations as opposed to typical points along the back edge of the convective region.

The profiles for cloud water and cloud ice were taken from Rutledge (1986). They are the same profiles used to represent a tropical convective cell; however, no better source of information was available for these profiles. This lack of information does not appear to be serious since the model simulations are not especially sensitive to the cloud water and cloud ice pro-

files. We do not include the transport of rain into the model domain as these particles are assumed to fall to the surface in the convective region of the squall line by virtue of their large fallspeeds.

In a parameterized model such as the one employed here, the specification of particle types (categories) entails assumptions of particle density and a relationship between particle size and fallspeed. Therefore, some physical interpretation of our ice particle categories, particularly graupel, is needed. The particles in the graupel category are considered to be relatively low-density, quasi-spherical particles with an assumed density of 0.3 g cm^{-3} . Ice particles with these characteristics most likely originate as vapor-grown crystals (or small frozen drops) and then grow by collecting supercooled water droplets at some stage. This interpretation of the graupel category in our model is consistent with the characteristics of graupel discussed by HH.

In addition to the transport of hydrometeors into the stratiform region from the convective region, water

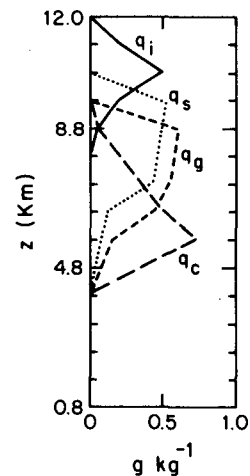


FIG. 4. Vertical profiles of graupel (q_g), snow (q_s), cloud ice (q_i) and cloud water (q_c) used as model input data.

vapor is advected into the stratiform region by the relative flow. Two different water vapor profiles have been used on the model boundary at $x = -40$ km. One profile represents the advection of unsaturated air (at the observed temperatures) into the model domain. This profile is taken directly from the OL data. The second profile assumes saturated air (with respect to water) at the observed temperatures to be flowing into the model domain. This saturated profile is considered to be the more likely case and is used in all the model simulations except for a sensitivity test in which we examine the effects of unsaturated air entering the model domain. We believe the OL data incorrectly indicates unsaturated conditions at $x = -40$ km because the data that entered the moisture composite for that location were relatively scarce as a result of poor radiosonde coverage in the vertical in the vicinity of the convective line and transition region. The profiles of unsaturated and saturated mixing ratios used as model input are shown in Fig. 5. The initial vapor field was set to these profiles throughout the model domain.

4. Simulations conducted

Eight different simulations were conducted as part of this study. Two simulations use the low-resolution rawinsonde-derived wind data from OL, and they include runs with convective cell hydrometeor profiles from Heymsfield and Hjermfelt (designated as HHOL) and no convective cell influx (NCOL). These two simulations were repeated using the Doppler radar wind data from SH, and they are designated as HSH and NCSH. Two additional simulations with the SH wind data were conducted to examine the effects of varying the graupel fallspeeds: in the HSH2 experiment the fallspeeds are doubled and in the HSH/2 experiment the fallspeeds are halved. The results obtained by eliminating the mesoscale updraft was tested in the HSHNU simulation. Finally, the HSHUN simu-

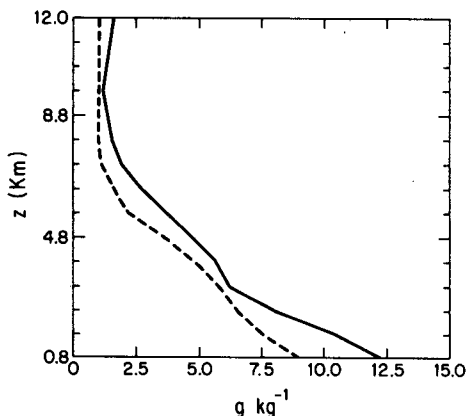


FIG. 5. Vertical profiles of water vapor mixing ratio used as model inputs. The saturated profile is denoted by solid line and the unsaturated profile by dashed line.

lation assumes the presence of unsaturated air along the inflow boundary (as discussed in section 3d). The description of these latter two simulations is confined to section 7.

Comparisons of the results of these simulations determine the model sensitivities to the different wind input data (OL versus SH) and thus the validity of the Smull and Houze (1985) hypothesis. The no-cell simulations isolate the effects of mesoscale vertical motions by eliminating advection of hydrometeors from the convective region into the stratiform region. Thus, the contributions of mesoscale vertical motions to the stratiform precipitation amounts can be examined.

5. Simulations using the low-resolution input data

In this section, the two model simulations using the low-resolution, sounding-derived input wind field, as shown in Fig. 2, will be discussed. Steady-state values of the various model output fields (reached after approximately 6000 s) will be presented.

a. HHOL simulation

The steady state fields of water vapor, cloud water and cloud ice are shown in Fig. 6. The strong effects of the kinematic flow field are particularly evident in the water vapor (q_v) and cloud water (q_c) fields. The q_v field responds to the stagnation region in the relative flow field (see Fig. 2a), and consequently builds up along a tilted axis extending from near the surface at $x = -42$ km to $x = -108$ km and $z = 4$ km. Rearward of this tilted maximum is a similar axis denoting a minimum in q_v . This region is associated with the inward and downward flow pattern (i.e., the mesoscale rear inflow), which transports low values of q_v downward. This has a strong effect on hydrometeor evaporation, as will be seen later.

Relatively large amounts of cloud water exist in the lower right-hand portion of the model domain (Fig. 6b). Condensation rates are large in this region due to the large water vapor content and to the upward motion in this region. Examining Fig. 2b, we see upward motion extending all the way to the surface in this area ($x = -40$ to -54 km). This structure, however, is an artifact of the low-resolution composite analysis of sounding data. The dual-Doppler data (Fig. 3b) show that actually downward, not upward, motion existed in this region. The erroneous upward motion in the low-resolution composite produces spurious condensation in this region. As will be seen later, this spurious cloud water leads to accretional growth and overprediction of precipitation rates in this area.

Cloud ice is confined to high levels (Fig. 6c). Cloud ice advected into the stratiform region from the convective region is quickly collected by snow and graupel. As will be confirmed in discussions below, the cloud ice in the region of $x < -70$ km is largely due to ice nucleation and growth in the mesoscale updraft region.

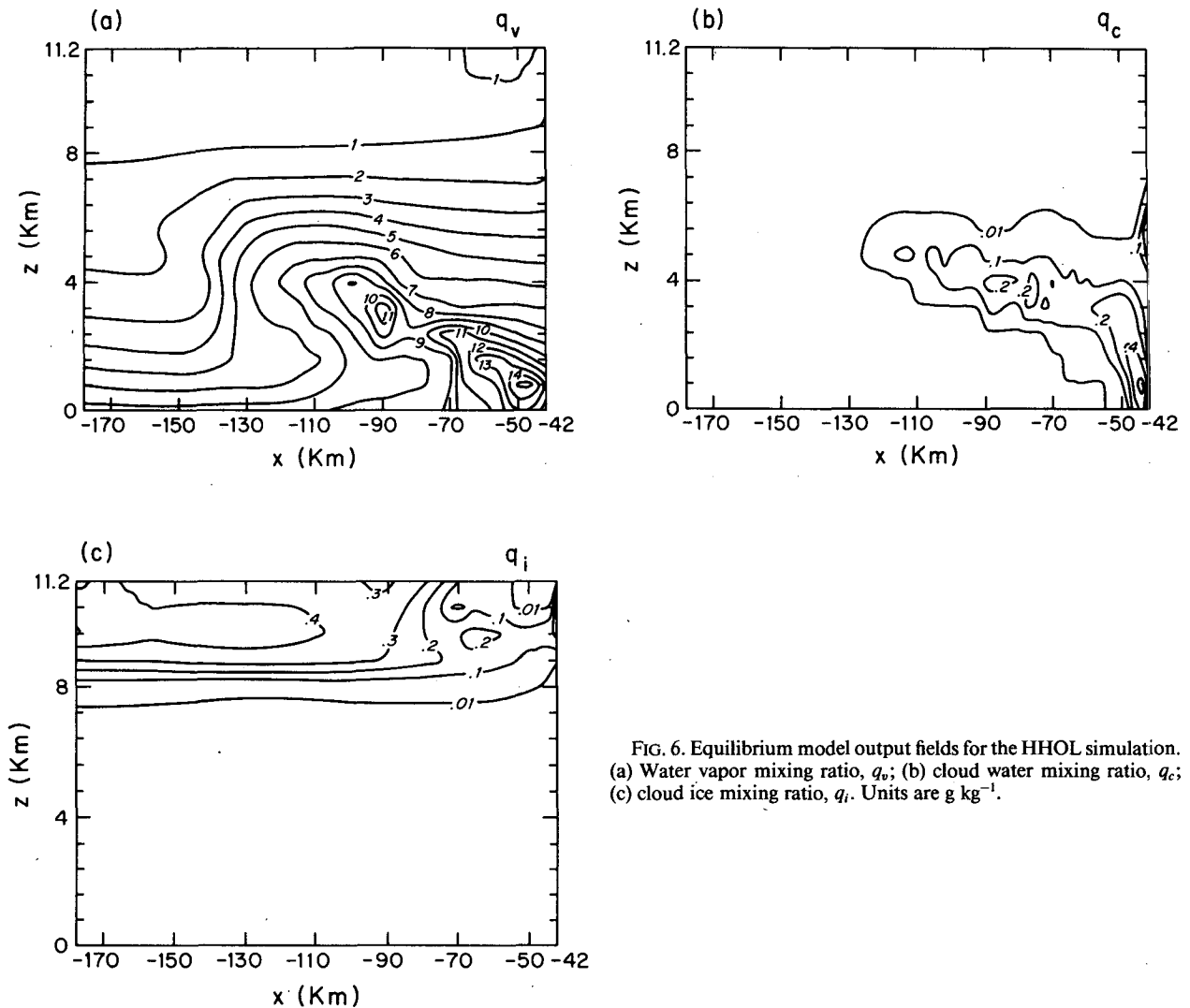


FIG. 6. Equilibrium model output fields for the HHOL simulation. (a) Water vapor mixing ratio, q_v ; (b) cloud water mixing ratio, q_c ; (c) cloud ice mixing ratio, q_i . Units are g kg^{-1} .

Maximum concentrations are 0.5 g kg^{-1} , which are similar to the values obtained in the tropical squall line simulation of Rutledge (1986).

The steady state field of snow (q_s), is shown in Fig. 7a. In the zone immediately behind the convective region ($x \approx -42$ to -75), there is a minimum, where snow is rapidly depleted as a result of collection by graupel. A broad maximum of q_s then appears, spanning nearly the entire model domain for $x < -70$ km. This snow is found to be a direct result of ice nucleation and subsequent autoconversion of cloud ice to snow. Continued growth occurs through vapor deposition. All of these processes are a result of the mesoscale updraft in this region (Fig. 2b).

In the graupel field (Fig. 7b), the fallout from the convective region is quite apparent, indicated by the steeply oriented isolines of q_g . To the rear of this area, say for $x < -80$ km, the q_g field is seen to be enhanced slightly. In the model, three independent processes may

initiate graupel. They involve collisions (followed by subsequent freezing) between rain and cloud ice, rain and snow, and snow and cloud water. However, none of these mechanisms are operative in this case. The first two processes require rain, which is absent above the 0°C level. For the third process, thresholds for snow and cloud water must be exceeded before graupel can be produced. These thresholds, set at 1.0 g kg^{-1} and 0.5 g kg^{-1} , respectively, were not reached, and graupel was thus not produced in the model domain. Therefore, all the graupel in the stratiform region was transported in from the convective region. The secondary maximum in the q_g content at $x = -100$ to -120 km is the result of graupel collecting snow, which was produced by the mesoscale ascent, and deposition growth. Nearly all of the graupel mass in this region was acquired within the mesoscale updraft. [The discontinuity in the q_g contours at the 4 km level near $x = -80$ km is associated with a change in the height of the 0°C level,

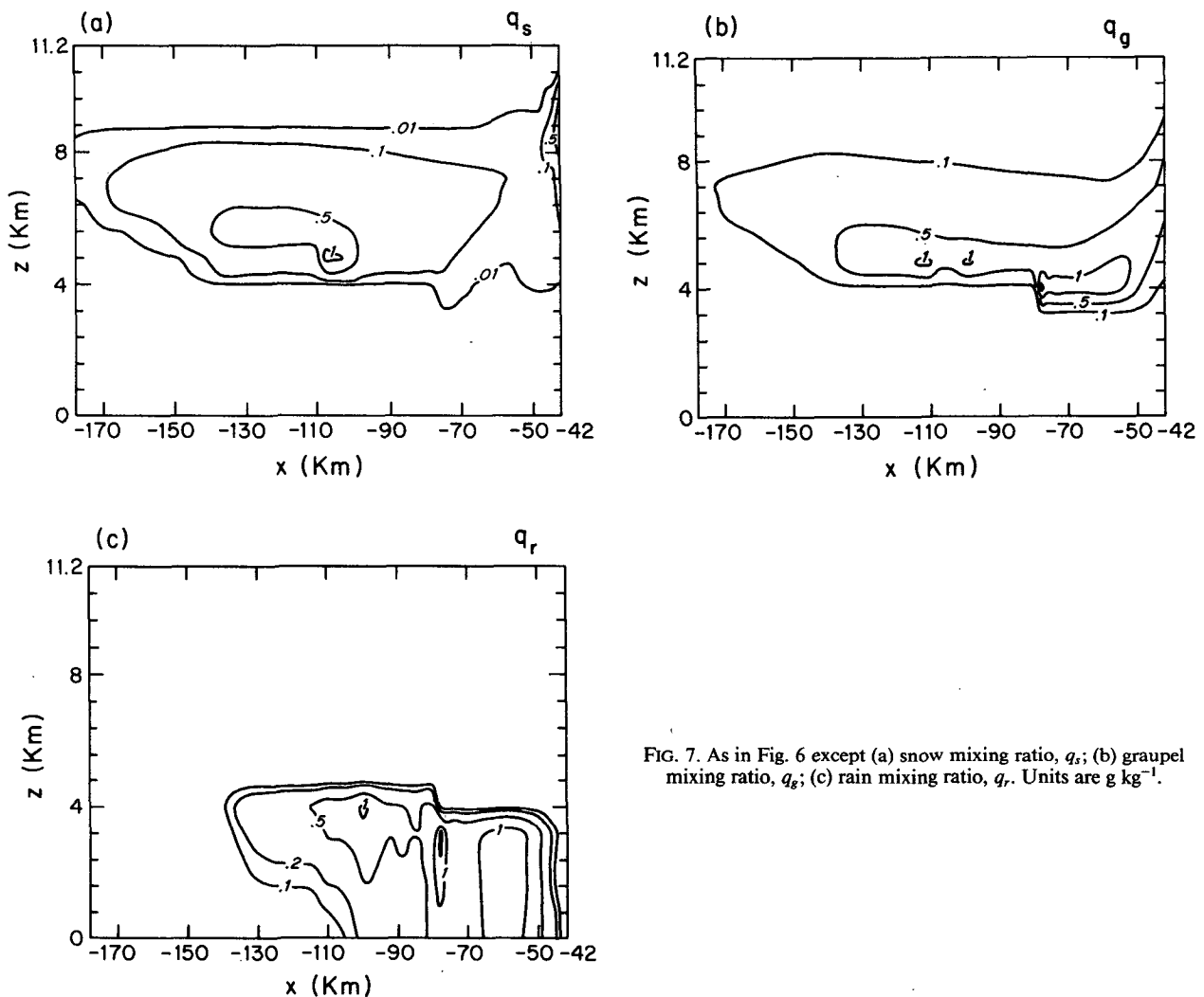


FIG. 7. As in Fig. 6 except (a) snow mixing ratio, q_s ; (b) graupel mixing ratio, q_g ; (c) rain mixing ratio, q_r . Units are g kg^{-1} .

the 0°C level being lower in the area of the heaviest precipitation. Similar discontinuities are also seen in other figures for this simulation.]

The rain in the stratiform region (Fig. 7c) is all initiated by the melting of snow and graupel. However, accretional growth and evaporation affect the overall distribution of q_r . Initiation of rain can occur below the 0°C level only if the threshold for autoconversion of cloud water (0.5 g kg^{-1}) is exceeded, and this does not occur. The largest values of q_r are found in the region for $-48 \text{ km} \leq x \leq -80 \text{ km}$, where rain results from the melting of graupel and is enhanced by accretional growth of rain below the 0°C level (where spurious cloud water was located as a result of spurious low-level updrafts in the low-resolution vertical velocity field). Smaller values of q_r are found for $x < -80 \text{ km}$. The rain in this region is directly associated with the fallout and melting of precipitation produced by the mesoscale updraft aloft. The overall q_r field in this simulation is very similar to the corresponding field dis-

cussed by Rutledge (1986), in particular his Fig. 17b. In that case, the higher values of q_r were associated with the fallout of graupel from the convective cells. This was followed by a region characterized by lighter, but widespread, precipitation. This latter precipitation region was due to precipitation generation by the mesoscale updraft. A very similar result holds here. However, one interesting contrast between the present study and that of Rutledge (1986) is in the overall width of the surface precipitation. In the tropical case, the surface precipitation zone was some 180 km in width, compared to approximately 90 km for the present simulation. The narrower precipitation zone in this mid-latitude case is attributable to a combination of two factors, a stronger mesoscale downdraft (resulting in larger evaporation rates) and pronounced rear-to-front flow which partly carried hydrometeors back toward the convective line, hence interrupting their rearward progress. This rear-to-front flow was not present in the case modeled by Rutledge (1986).

The precipitation rate in the x - z plane for the HHOL case is shown in Fig. 8. The largest precipitation rates are coincident with the q_r maxima below the 0°C level (Fig. 7c). The largest surface precipitation rates in this area are between 20 and 25 mm h^{-1} and are associated with the fallout of melted graupel emanating from the upper levels of the convective region. These precipitation rates are most likely erroneously high because the spurious cloud water at low levels (discussed in section 5a) allowed accretional growth of the rain to occur from the 0°C level to the surface, which is quite unrealistic. The diagnosed surface precipitation does not agree with the observed pattern. For example, the observed radar reflectivity indicates a *minimum* 30–50 km behind the convective region which is then trailed by a region of light precipitation. The model, on the other hand, produces a *maximum* in the surface precipitation rate in this region. The precipitation pattern discussed by Rutledge (1986), for the tropical squall line, was very similar to that in Fig. 8 (cf. his Fig. 18b). Apparently, the composites of relative air motion derived from rawinsonde data by OL and Gamache and Houze (1982) do not have sufficient detail to allow for a very realistic diagnosis of the cloud and precipitation pattern in the region immediately to the rear of the convective line (the transition zone). Later, when we examine the simulations with the more detailed SH wind data, we will see a precipitation pattern that is in much better agreement with observations.

Shown in Fig. 9 is the radar reflectivity in dBZ for the HHOL simulation. Below the freezing level we calculated the radar reflectivity from the relationship of Marshall and Palmer (1948),

$$\text{dBZ} = 16 \log_{10}(\rho q_r) + 23.01 \quad (2)$$

where ρ is the density of air. Above the 0°C level we applied a relationship of the form,

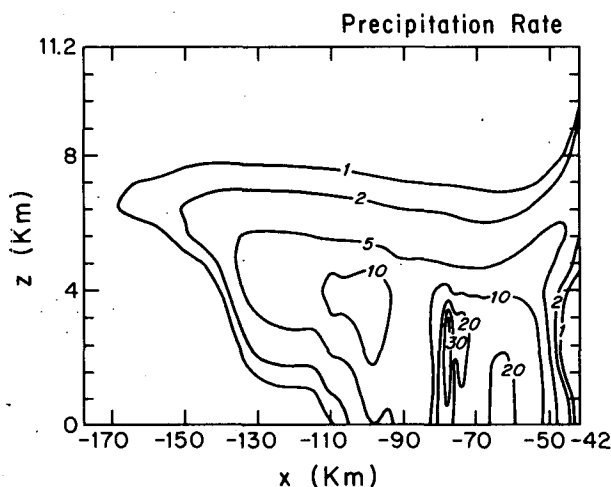


FIG. 8. Equilibrium precipitation for the HHOL simulation. Units are mm h^{-1} .

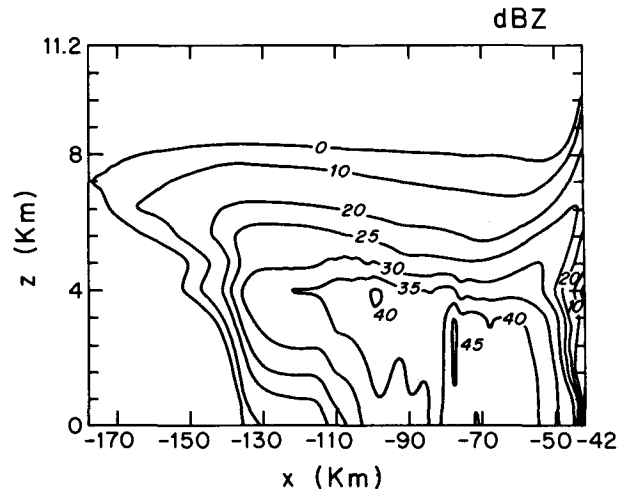


FIG. 9. Diagnosed radar reflectivity field (dBZ) for the HHOL simulation.

$$\text{dBZ}_e = 25.6 \log_{10}(\rho q_t) + 33.0 \quad (3)$$

derived by Heymsfield and Palmer (1985) from observations of anvil clouds associated with thunderstorms. The term q_t is the total ice mixing ratio ($q_s + q_g$). We neglect the reflectivity due to both cloud water and cloud ice.

We note interesting comparisons between the model reflectivity and precipitation pattern with similar observed fields (indicated in Fig. 10 of Smull and Houze, 1985). The location of the back edge of the observed radar echo at the surface (~ 20 dBZ at these ranges) agrees well with the model results; the back edge is found at $x = -110$ km in both the model results and observations. Also, an upper-level, nonprecipitating anvil is present in both the observations and model results. We find this upper-level anvil to be produced by the growth of ice generated within the mesoscale updraft region. The precipitation from this region largely sublimates prior to melting. This result is consistent with upper-level ice streaks, or virga, which we often observed in similar regions during the passage of squall lines in Kansas during the PRE-STORM project in May–June 1985.

b. NCOL simulation

The NCOL simulation was conducted to test the ability of the mesoscale updraft to produce precipitation without any influx of hydrometeors from the convective region. The hydrometeor flux from the convective region was set to zero for this simulation, while all other model inputs and parameters were unchanged from the HHOL case.

The water vapor, cloud water, and cloud ice fields in the NCOL case were very similar to those in the HHOL simulation. In particular, the cloud ice content for the NCOL simulation is nearly identical to that

seen in the HHOL case (Fig. 6c). Hence, we conclude that the presence of cloud ice in the HHOL case (and in the actual storm's stratiform region) is due to generation in the mesoscale updraft, which maintains ice saturation in this region, thus allowing nucleation and growth of ice crystals.

The snow and rain mixing ratios are shown in Fig. 10. Graupel is absent in this simulation since conditions were not achieved for its initiation in the stratiform region and none is advected into the domain in this simulation. Rather, large amounts of snow are generated by the mesoscale updraft (Fig. 10a). The snow is generated above the 8 km level through the conversion of cloud ice to snow (PCONV). This process is similar to the autoconversion term for cloud water to rain, i.e., the cloud ice is converted to snow when a minimum cloud ice threshold is exceeded (details in Rutledge and Hobbs, 1983). Once the snow is initiated by conversion, continued growth takes place through vapor deposition. Growth by riming and cloud ice collection were both unimportant. Melting commences near the 4 km level.

The rain field is shown in Fig. 10b. In this simulation, rain is produced solely by the melting of snow and may therefore be regarded as a direct result of the mesoscale updraft. For $x > -80$ km the values of q_r are considerably lower than the values of q_r shown in Fig. 7c for the HHOL simulation. This region is where the bulk of the hydrometeors advected into the stratiform region from the convective region in the HHOL case reach the surface. For $x < -80$ km, both the HHOL and NCOL simulations show the same q_r distribution. From this result, we conclude that in this region precipitation in both cases is only due to the mesoscale updraft because particles from the convective line reach the surface prior to this point. Evaporation erodes the back edge of the precipitation region as the precipitation falls directly into the relatively dry rear-to-front flow.

The precipitation rate in the x - z plane for this simulation is displayed in Fig. 11. Precipitation rates at the surface are mainly less than 10 mm h^{-1} . The region of heaviest precipitation (near $x = -86$ km) is a result of the cloud water content in this region allowing accretional growth. Since the cloud water content here is an artifact of the low-resolution composite vertical velocity field, this feature is probably fictitious. The anvil-like precipitation structure in the left part of the domain reflects the effect of evaporation on the precipitation at lower levels. From this simulation, we see that the mesoscale vertical motion field can sustain light precipitation at the surface in the absence of hydrometeors advected from the convective region.

6. Simulations using the high-resolution input data

In this section, we examine results obtained using the high-resolution input winds derived from dual-Doppler radar by Smull and Houze (1986).

a. The HSH simulation

In this simulation we have combined the hydrometeor mass profiles shown in Fig. 4 with the SH kinematic data shown in Fig. 3. The diagnosed temperature field for the HSH case is shown in Fig. 12. This field exhibits only weak horizontal gradients. The 0°C level is located at approximately the 4-km level.

The fields of water vapor, cloud water and cloud ice are shown in Fig. 13. In Fig. 13a the effects of the downward transport of water vapor in the transition zone ($x = -50$ to $x = -80$ km) are indicated by the downward bowing of the q_v isolines at low levels. The cloud water (q_c) field (Fig. 13b) is found to be considerably different from the q_c field in the HHOL case (Fig. 6b). The cloud water in the region behind the

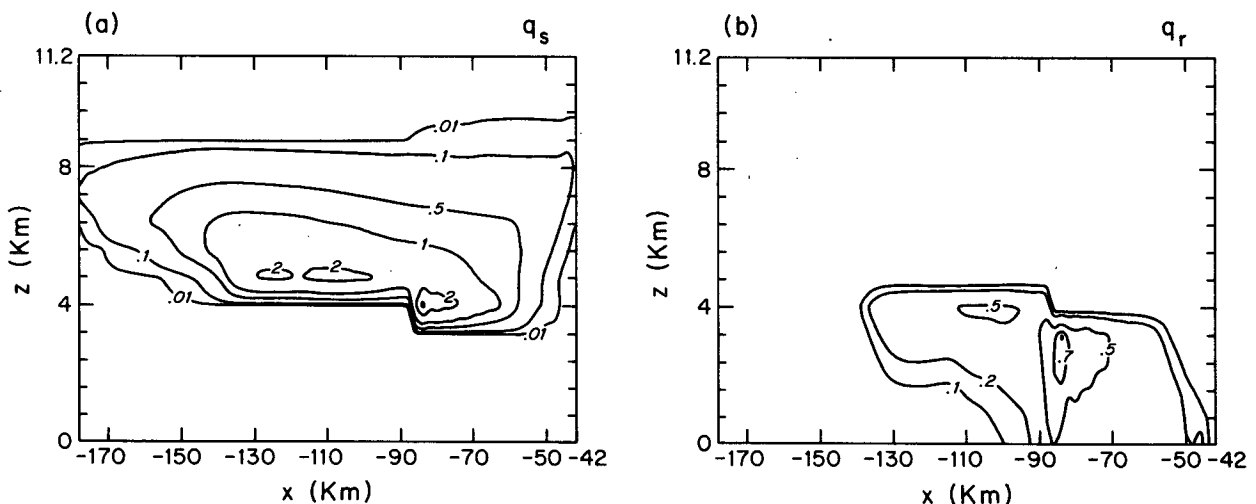


FIG. 10. Equilibrium model output fields for the NCOL simulation. (a) Snow mixing ratio, q_s ; (b) rain mixing ratio, q_r . Units are g kg^{-1} .

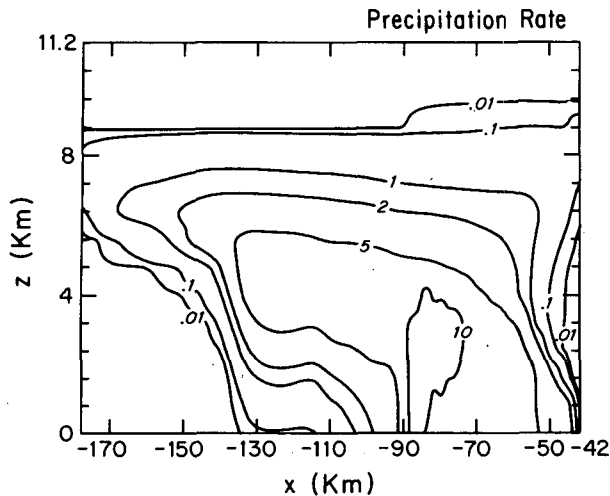


FIG. 11. Equilibrium precipitation rate for the NCOL simulation. Units are mm h^{-1} .

convective line ($x = -55$ to -70 km) is now absent, as a result of the sinking motion shown to be there in the radar data. In fact, only a small amount of cloud water is found in the HSH case. It is centered around the 0°C level and is generated by cooling associated with melting hydrometeors. The q_i field, shown in Fig. 13c, is quite similar to the same field in the HHOL case (Fig. 6c). This result is expected since the vertical motion and temperature fields are similar in this region in the two cases. Most of the cloud ice is found to be generated by the mesoscale updraft (further discussion below).

The precipitation fields, q_s , q_g and q_r , are shown in Fig. 14. The snow (q_s) content (Fig. 14a) decreases rapidly over a short distance immediately behind the convective line, where it is collected by graupel. Snow is present throughout most of the domain, however. At $x < -60$ km, q_s is largely generated by the mesoscale updraft.

The graupel content (q_g) is displayed in Fig. 14b. The isolines of q_g suggest a streamer of graupel trailing from the upper levels of the convective region, diffusing somewhat, and spanning nearly the entire domain, as a result of the strong horizontal flow in the SH case (Fig. 3a). This pattern of fallout of ice particles originating in the convective line is consistent with the pattern estimated by Smull and Houze (1985). The fall velocities of graupel in the model ($1.5\text{--}2\text{ m s}^{-1}$) are well within the range of those assumed by Smull and Houze (1985) to calculate their trajectories (Fig. 1c). This range of fall velocities, combined with the front-to-rear jet of horizontal relative wind, which was most pronounced just to the rear of the convective line, led to the transport of the graupel across the domain.

The field of rain mixing ratio (q_r) in Fig. 14c is consistent with the graupel field in Fig. 14b. As the graupel is advected into the region from the upper portions of

the convective line and is carried across the domain, it melts and falls to the surface, thus producing the region of enhanced stratiform rain seen below the melting layer in the stratiform portion of the storm [Fig. 1; Fig. 3 of SH]. The model fields of precipitation rate and radar reflectivity (Fig. 15) indicate this region of enhanced stratiform precipitation as a 20–25 km wide maximum at the surface (bounded roughly by contours of 4 mm h^{-1} rain rate and 30 dBZ echo intensity) directly traceable back to the convective cell influx emanating from upper levels along the $x = -50$ km boundary with the convective region. This result confirms Smull and Houze's (1985) hypothesis that the width and horizontal position of the most intense portion of the trailing stratiform precipitation can be explained by the pattern of fallout of particles advected into the stratiform region from the convective region.

b. The NCSH simulation

For this simulation, all model inputs and initial conditions were the same as in the HSH case, except that the influx of hydrometeor mass from the convective region was set to zero.

The resulting fields of temperature and water vapor were essentially unchanged from those shown in the HSH case. As in the HSH case (Fig. 13b), small amounts of cloud water were present. The precipitation, although weaker in this case, still produces large enough cooling rates (associated with melting near the 0°C level) to produce water-saturated conditions and the presence of cloud water. The cloud ice field is virtually identical to that shown for the HSH case which was displayed in Fig. 13c. The bulk of the cloud ice depicted in that figure is generated by the mesoscale updraft, as the cloud ice that enters the domain from

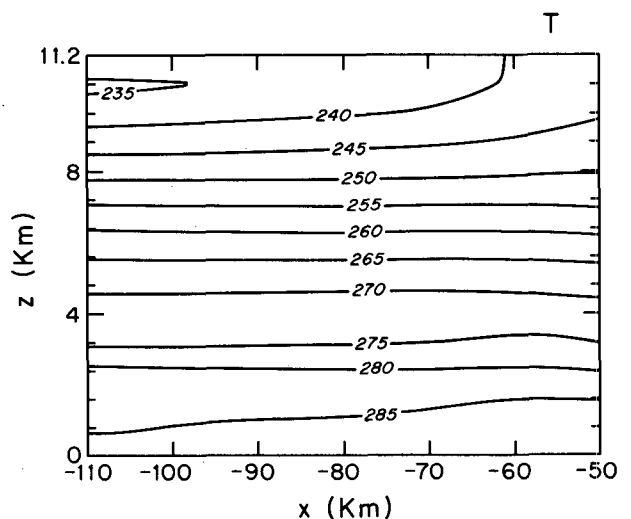


FIG. 12. The equilibrium temperature field for the HSH simulation in K.

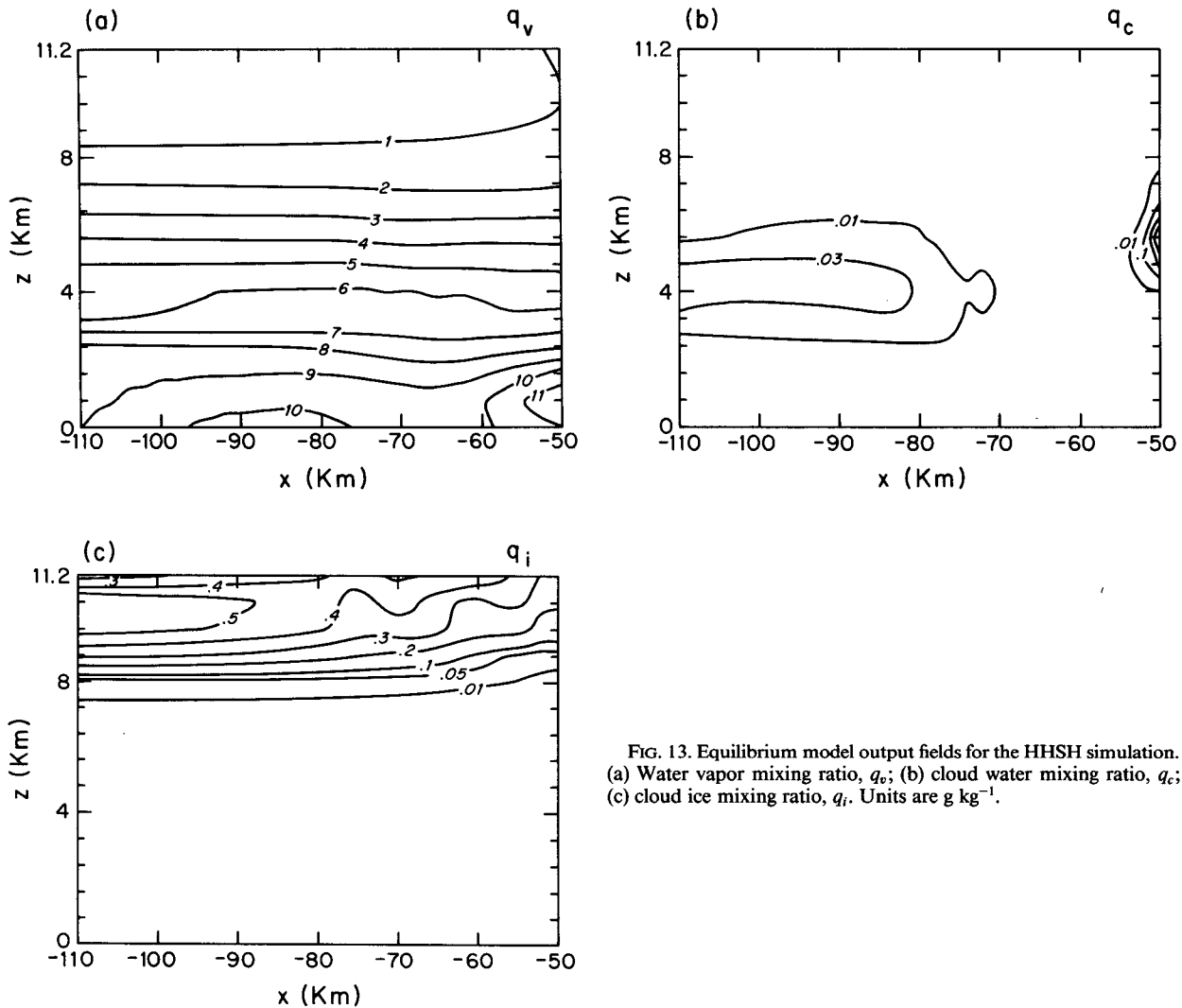


FIG. 13. Equilibrium model output fields for the HSH simulation. (a) Water vapor mixing ratio, q_v ; (b) cloud water mixing ratio, q_c ; (c) cloud ice mixing ratio, q_i . Units are g kg^{-1} .

the convective region is rapidly removed through collection by snow and graupel.

The snow and rain contents for the NCSH case are shown in Fig. 16. Relatively large amounts of snow are present in the NCSH case (Fig. 16a). The equilibrium q_s content is larger in this case since graupel is not present to remove snow by collection. Such collection kept the q_s content relatively small in the HSH case. The snow generation occurs through the conversion of cloud ice, followed by continued depositional growth from the vapor phase. The fallout and melting of this snow produces only weak surface precipitation. The rain content (q_r) is displayed in Fig. 16b. We find in the NCSH case that the mesoscale updraft produces little surface precipitation within the model domain. These findings confirm our earlier argument that the precipitation reaching the surface in the HSH case is a result of the hydrometeor influx from the convective cell although, as will be discussed later, a substantial

amount of mass is added to these hydrometeors through the collection of condensate produced by the mesoscale updraft. The precipitation rate for this simulation is presented in Fig. 17. Maximum snowfall rates reach 4 mm h^{-1} . Surface rainfall rates are less than 0.5 mm h^{-1} within the model domain as a result of strong evaporation in the mesoscale downdraft. Although it is difficult to extrapolate the model results beyond the model domain, it is doubtful that the surface rain rates could be very significant in the presence of mesoscale subsidence at mid- to low levels.

c. Sensitivity to graupel fallspeeds

In this section we briefly discuss two simulations that examine the sensitivity of the location of the surface precipitation band to the graupel fallspeed values. These simulations were identical to the HSH case except in HSH2, where graupel fallspeeds are doubled, and in HSH/2, graupel fallspeeds are halved.

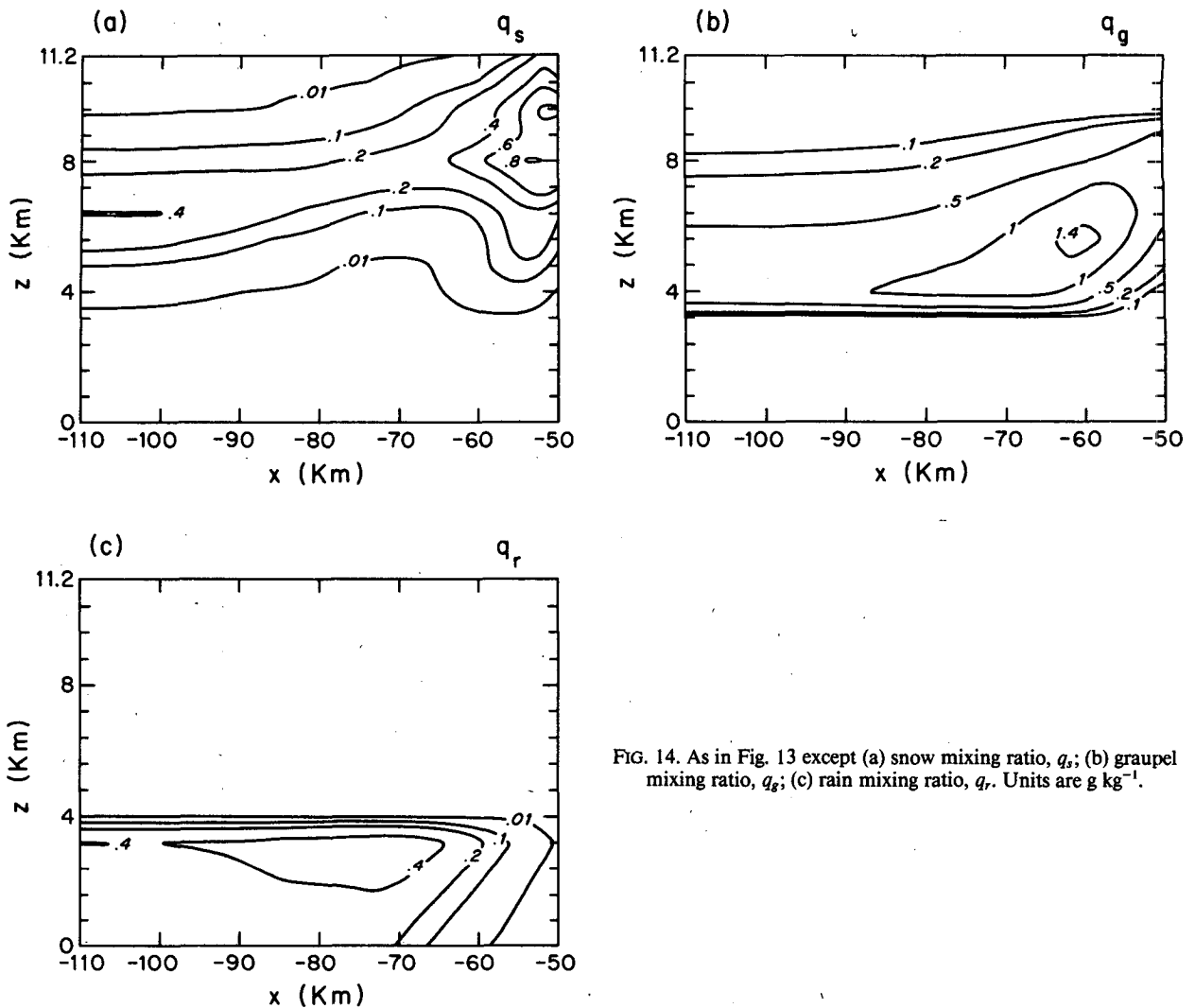


FIG. 14. As in Fig. 13 except (a) snow mixing ratio, q_s ; (b) graupel mixing ratio, q_g ; (c) rain mixing ratio, q_r . Units are g kg^{-1} .

For the HSH2 case, we found a narrower band, located closer to the convective cells, characterized by larger surface precipitation rates ($\sim 7\text{--}9 \text{ mm h}^{-1}$) compared to both the HSH simulation and observations. Because of the larger fallspeeds in this case (-2 to 4.5 m s^{-1} compared to -1 to -2 m s^{-1} in the HSH case) the graupel diffuses less and falls to the surface closer to the cell, destroying the observed "transition zone," located between $x = -50$ and $x = -70 \text{ km}$.

The opposite effect is seen when the fallspeed of graupel is decreased by a factor of 2 (HSH/2). In this case, as a result of low graupel fallspeeds (-1.0 to -1.3 m s^{-1}), the distinct surface precipitation band was not found. In fact, the heaviest precipitation began near the extreme left portion of the model grid.

The location and width of the surface precipitation band is found to be critically dependent on the graupel trajectories, and hence on the assumed particle fallspeeds. Our model simulations indicate that moderately dense graupel-like particles with fallspeeds in the

range $1\text{--}2 \text{ m s}^{-1}$ best explain the position of the enhanced stratiform precipitation. The existence of such particles in the convective cells supplying hydrometeors to the stratiform region is indicated by the data of HH. However, it should be noted that if graupel particles or snowflakes were advected into the stratiform region at a lower altitude than suggested by the HH profile (Fig. 4), then the location and width of the band of maximum stratiform precipitation at the surface would be explained by particles with lower fallspeeds ($\sim 1 \text{ m s}^{-1}$). Further study of the vertical profile of hydrometeors advected into the stratiform region is needed.

7. Water budget

In section 6, we established that the location and width of the stratiform rain is determined primarily by the pattern of fallout of hydrometeors advected into the stratiform region from the convective region. Given this result, what is the role of the mesoscale ascent in

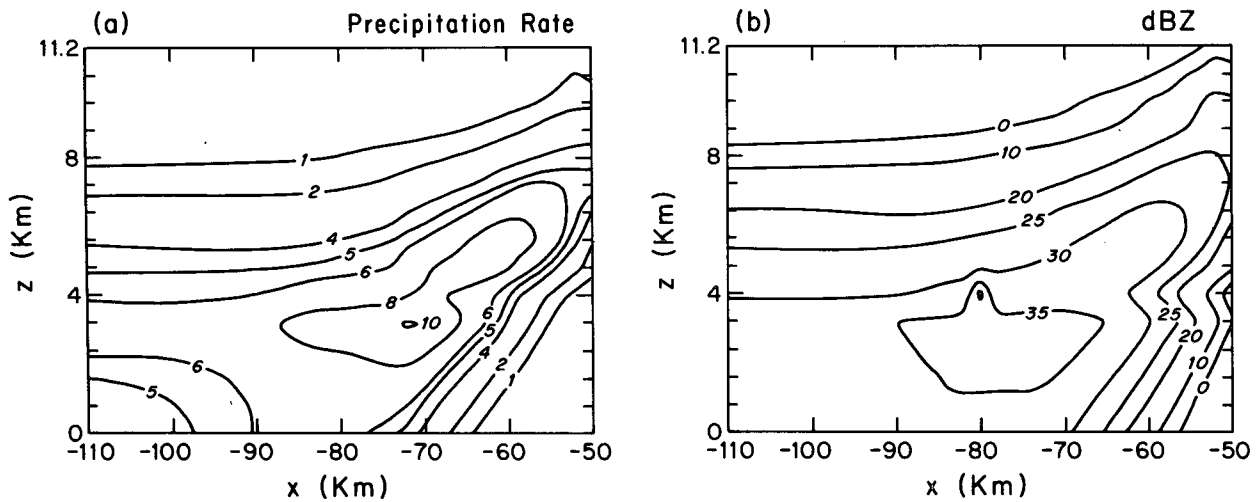


FIG. 15. Diagnosed fields of precipitation rate and radar reflectivity for the HSH simulation. (a) Precipitation rate in mm h^{-1} , (b) radar reflectivity in dBZ.

the stratiform cloud? Is the “stratiform rain” really just convective condensate (debris) that has been blown downwind from the convective line, or does the mesoscale updraft motion in the cloud through which the convective hydrometeors pass enhance the precipitation process? In this section, we address these questions by examining the water budget of the stratiform region implied by our model calculations.

Following Gamache and Houze (1983), we express the water budget for the model domain as

$$R_m = C_{mu} - E_{md} - T + C_A, \quad (4)$$

where R_m is the surface precipitation in the model domain, C_A is the mass of condensate advected into the

domain from the convective region by the relative flow, C_{mu} is the net mass of water condensed in the region occupied by the mesoscale updraft, and T is the mass lost by outflow through the left boundary of the model domain. (This term was called E_{me} by Gamache and Houze, 1983.) Here E_{md} is the net evaporation in the region of the mesoscale downdraft.

The terms in the water budgets computed are presented for four of our model simulations in Table 1. Also shown are values obtained from data, without the aid of a diagnostic model, by Gamache and Houze (1983) and Chong (1983). Their terms have been normalized to reflect a case in which C_A has a value of 44 units, so that they can be compared directly with our model results. In comparing the water budget of the

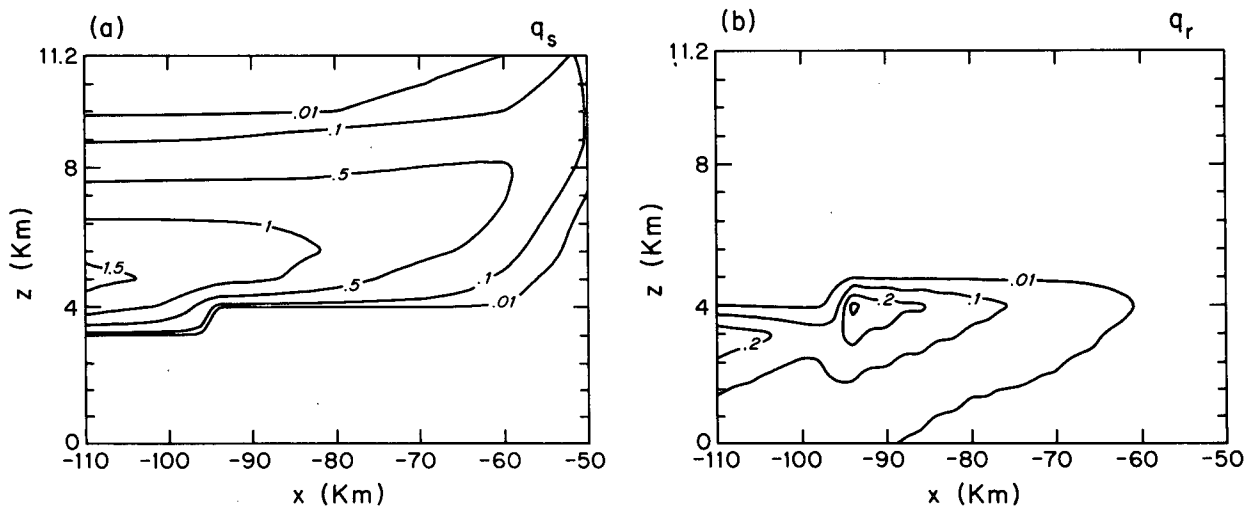


FIG. 16. Equilibrium model output fields for the NCSH simulation. (a) Snow mixing ratio, q_s ; (b) Rain mixing ratio, q_r . Units are g kg^{-1} .

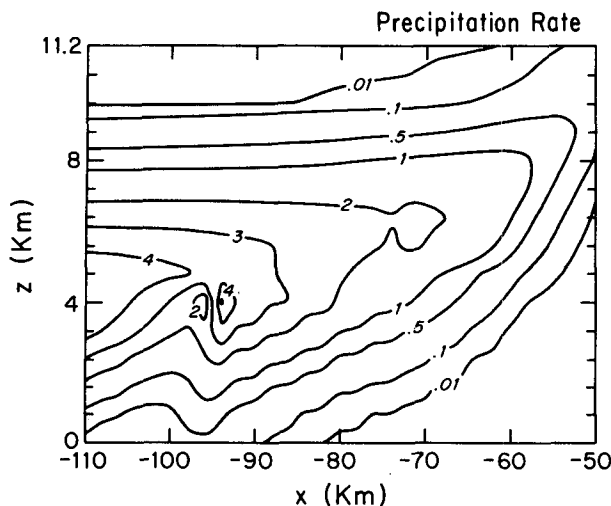


FIG. 17. Equilibrium precipitation rate for the NCSH simulation. Units are mm h^{-1} .

HSSH simulation, which we consider to be the most realistic of our cases, to the results by Gamache and Houze (1983) and Chong (1983), we note that their values of C_{mu} , E_{md} , T and R_m differ by as much as a factor of four from those of the HSSH simulation. We are not alarmed at these differences since our case represents a midlatitude continental storm, while Gamache and Houze's (1983) case was an oceanic tropical squall line and Chong's (1983) was a continental tropical squall system. These widely differing environments suggest the possibility of various intensities. Here the midlatitude continental case (HSSH) appears most intense (largest C_{mu} and E_{md}), while the oceanic tropical case (Gamache and Houze, 1983) was least intense (smallest C_{mu} and E_{md}). The continental tropical case appears to have been of intermediate intensity.

Insight into the roles of the mesoscale ascent and horizontal influx of condensate from the convective region is achieved by way of the model water budgets for the cases in which the mesoscale updraft is set to zero (HSSHNU) and the influx of hydrometeors from the convective region is shut off (NCSH). Values of the water budget parameters for these two cases are indicated in Table 1. They show that most surface precipitation (43 units) is obtained when both processes act together (hydrometeor influx and mesoscale updraft). For the case of no influx of hydrometeors from the convective region (NCSH), the stratiform region is unable to produce a significant amount of surface rainfall (only 2 units). A substantial amount of precipitation does fall from the midlevel cloud base in this case; however, little of it survives passage through the mesoscale downdraft located below the stratiform cloud ($E_{md} = 23$ units). Much is transported off the model grid ($T = 56$ units). This transport term is important

in that it would most likely give rise to an extensive nonprecipitating anvil cloud. For the case in which there is no mesoscale updraft, some rain reaches the surface (11 units), yet only about one-fourth as much as when both processes act together. In this case most of the hydrometeor influx evaporates in the mesoscale downdraft. For the case where unsaturated air flows into the stratiform region (HSSHUN), we find no surface rainfall. Condensation in the mesoscale updraft is much less as a result of the lower supply of water vapor while evaporation in the mesoscale downdraft is quite large.

Clearly the amount of stratiform rain is greatest when both processes act together. In this case, the graupel and snow particles advected into the stratiform region from the convective region feed upon moisture made available by the mesoscale updraft. More importantly, the influx of hydrometeors appears to be necessary before condensate produced by the mesoscale updraft can be removed and therefore contribute to the surface rainfall. In this sense we view the precipitation in the stratiform region as a seeder-feeder process. In this case we find that approximately 20% of the surface precipitation in the stratiform region is due to the influx of hydrometeors from the convective line. The remaining 80% is due to condensation produced by the mesoscale updraft. Within the area of the mesoscale updraft, vapor deposition and the collection of snow generated by the mesoscale updraft contribute nearly equally to the growth of graupel carried into the stratiform region. Growth of graupel by collecting cloud ice generated by the mesoscale updraft is not important.

8. Conclusions

By conducting diagnostic model calculations of the steady state configurations of cloud microphysical and thermodynamic processes consistent with mesoscale air motions observed by Doppler radar in the trailing

TABLE 1. Values of the water budget components. Results of model simulations are denoted by HSSH, NCSH, HSSHNU and HSSHUN, as explained in the text. The values in the GH categories are from Gamache and Houze (1983) and are based on observations of an oceanic tropical squall line. The data from Chong (1983) are based on observations of a continental tropical squall line. All terms have units of $\text{kg m}^{-1} \text{s}^{-1}$, where the length unit is the unit distance perpendicular to the model x - z domain.

Case	$R_m =$	C_{mu}	$-E_{md}$	$-T$	$+C_A$
HSSH	43 =	87	-48	-40	44
NCSH	2 =	81	-23	-56	0
HSSHNU	11 =	5	-37	-1	44
HSSHUN	0 =	47	-55	-37	44
GH Case I	51 =	37	-17	-13	44
GH Case II	42 =	22	-14	-10	44
Chong (1983)	19 =	50	-52	-23	44

stratiform region of the 22 May 1976 Oklahoma squall line, we have confirmed the hypothesis of Smull and Houze (1985) that the breadth and horizontal position of the most intense portion of the trailing stratiform precipitation is explained by the pattern of fallout of hydrometeors advected into the stratiform region by the mesoscale airflow relative to the storm. Graupel particles from the upper portions of cells in the convective line fall at $1\text{--}2\text{ m s}^{-1}$ while they are swept rearward by the horizontal relative wind. The result is that by the time they reach the melting level and fall out as rain, they are concentrated over a 30 km wide region. This region is the zone of heaviest stratiform rain.

The hydrometeors flowing into the model domain from the convective region pass through the upper-level mesoscale updraft of the trailing stratiform cloud as they make their long sloping descent to the melting level. During this passage, the graupel particles from the cells accumulate water mass made available by the mesoscale updraft. The graupel grows by vapor deposition and collects snow generated by the mesoscale ascent. Water budget calculations show that without the mesoscale updraft, only about one-fourth as much rain would reach the surface in the stratiform region, while without the influx of hydrometeors from the cells, almost no rain would reach the surface.

Apparently, the influx of hydrometeors into the stratiform region is crucial. Not only does their pattern of fallout determine the width and location of the most intense stratiform rain, but without them, it is likely that no significant precipitation would reach the ground. The model calculations based on Doppler radar derived air motions show that the mesoscale updraft substantially enhances the amount of rain reaching the surface in this region of maximum stratiform precipitation by providing vapor and condensate upon which the inflowing ice particles can feed and thereby increase their mass.

Model calculations based on lower-resolution but more areally extensive composite sounding data show that the mesoscale updraft also accounts for the thick stratiform cloud that extends far to the rear of the surface rain area. Precipitation generated by the mesoscale ascent falls from the base of the rearward extension of the mesoscale cloud system but evaporates before reaching the surface. Higher humidity below cloud base would permit some of this mesoscale updraft generated precipitation to reach the surface [e.g., the tropical case simulated by Rutledge (1986)].

Acknowledgments. Dr. Bradley F. Smull supplied the dual-Doppler radar data from which the air motion fields were derived. Dr. Andrew J. Heymsfield provided the microphysical data and gave helpful comments regarding their interpretation. He is also acknowledged for his many helpful comments and discussions. We thank Dean Vickers for help with computing, Michelle

Burrier for typing the manuscript and Linda Hagarth for preparing the figures. The reviewers are also acknowledged for their comments, which led to improvements in the manuscript. This research was supported by the National Science Foundation under grants ATM-8317466, ATM-8413542, and ATM-8521403, and by the Scientific Computing Division of the National Center for Atmospheric Research.

REFERENCES

- Atlas, D., K. R. Hardy, R. Wexler and R. J. Boucher, 1963: On the origin of hurricane spiral rainbands. *Geophys. Int.*, **3**, 123–132.
- Barnes, G. M., and K. Sieckman, 1984: The environment of fast- and slow-moving tropical mesoscale convective cloud lines. *Mon. Wea. Rev.*, **112**, 1782–1794.
- Chong, M., 1983: Les radars météorologiques Doppler pour l'étude de la convection orageuse: Application à l'étude d'une ligne de grains tropicale. Thèse de Doctorat d'Etat, Université de Paris VI, 140 pp.
- Fujita, T. T., 1955: Results of detailed synoptic studies of squall lines. *Tellus*, **7**, 405–436.
- Gamache, J. F., and R. A. Houze, Jr., 1982: Mesoscale air motions associated with a tropical squall line. *Mon. Wea. Rev.*, **110**, 118–135.
- , and —, 1983: Water budget of a mesoscale convective system in the tropics. *J. Atmos. Sci.*, **40**, 1835–1850.
- , and —, 1985: Further analysis of the composite wind and thermodynamic structure of the 12 September GATE squall line. *Mon. Wea. Rev.*, **113**, 1241–1259.
- Hamilton, R. A., and J. W. Archbold, 1945: Meteorology of Nigeria and adjacent territory. *Quart. J. Roy. Meteor. Soc.*, **71**, 231–264.
- Hauser, D., and P. Amayenc, 1986: Retrieval of cloud water and water vapor contents from Doppler radar data in a tropical squall line. *J. Atmos. Sci.*, **43**, 823–838.
- Heymsfield, A. J., and M. R. Hjermfelt, 1984: Processes of hydrometeor development in Oklahoma convective clouds. *J. Atmos. Sci.*, **41**, 2811–2835.
- , and A. G. Palmer, 1985: Relationships for deriving thunderstorm anvil ice mass for CCOPE storm water budget estimates. *J. Climate Appl. Meteor.*, **25**, 691–702.
- Houze, R. A., Jr., 1977: Structure and dynamics of a tropical squall-line system. *Mon. Wea. Rev.*, **105**, 1540–1567.
- , 1981: Structures of atmospheric precipitation systems: A global survey. *Radio Sci.*, **16**, 671–689.
- , and E. N. Rappaport, 1984: Air motions and precipitation structure of an early summer squall line over the eastern tropical Atlantic. *J. Atmos. Sci.*, **41**, 553–574.
- Lord, S. J., H. F. Willoughby and J. M. Pietrowicz, 1984: Role of parameterized ice-phase microphysics in an axisymmetric, non-hydrostatic tropical cyclone model. *J. Atmos. Sci.*, **41**, 2836–2848.
- Marshall, J. S., and W. Palmer, 1948: The distribution of raindrops with size. *J. Meteor.*, **5**, 165–166.
- Newton, C. W., 1950: Structures and mechanisms of the prefrontal squall line. *J. Meteor.*, **7**, 210–222.
- Ogura, Y., and M. T. Liou, 1980: The structure of a midlatitude squall line: A case study. *J. Atmos. Sci.*, **37**, 553–567.
- Pedgley, D. E., 1962: A mesosynoptic analysis of the thunderstorms of 28 August 1958. *Brit. Meteor. Off., Geophys. Mem.*, No. 106, 74 pp.
- Pruppacher, H. R., and J. D. Klett, 1978: *Microphysics of Clouds and Precipitation*. Reidel, 714 pp.
- Rutledge, S. A., 1986: A diagnostic numerical study of the stratiform region associated with a tropical squall line. *J. Atmos. Sci.*, **43**, 1337–1358.

- , and P. V. Hobbs, 1983: The mesoscale and microscale structure and organization of clouds and precipitation in midlatitude cyclones. Part VIII: A model for the "seeder-feeder" process in warm-frontal rainbands. *J. Atmos. Sci.*, **40**, 1185–1206.
- , and —, 1984: The mesoscale and microscale structure and organization of clouds and precipitation in midlatitude cyclones. Part XII: A diagnostic modeling study of precipitation development in narrow cold-frontal rainbands. *J. Atmos. Sci.*, **41**, 2949–2972.
- Smull, B. F., and R. A. Houze, Jr., 1985: A midlatitude squall line with a trailing region of stratiform rain: Radar and satellite observations. *Mon. Wea. Rev.*, **113**, 117–133.
- , and —, 1986: Dual-Doppler radar analysis of a midlatitude squall line with a trailing region of stratiform rain. *J. Atmos. Sci.*, **44**, 2128–2148.
- Sommeria, G., and J. Testud, 1984: COPT81: A field experiment designed for the study of dynamics and electrical activity of deep convection in continental tropical regions. *Bull. Amer. Meteor. Soc.*, **65**, 4–10.
- Srivastava, R. C., T. J. Matejka and T. J. Lorello, 1986: Doppler radar study of the trailing anvil region associated with a squall line. *J. Atmos. Sci.*, **43**, 356–377.
- Wei, T., and R. A. Houze, Jr., 1986: The GATE squall line of 9–10 August 1974. (Accepted for publication in *Advances in Atmospheric Sciences*, Academia Sinica, Beijing).
- Zipser, E. J., 1969: The role of organized unsaturated convective downdrafts in the structure and rapid decay of an equatorial disturbance. *J. Appl. Meteor.*, **8**, 799–814.
- , 1977: Mesoscale and convective-scale downdrafts as distinct components of squall-line structure. *Mon. Wea. Rev.*, **105**, 1568–1589.